nature photonics

Article

https://doi.org/10.1038/s41566-023-01178-0

Entanglement-enhanced optomechanical sensing

Received: 2 November 2022

Accepted: 17 February 2023

Yi Xia[1,2], Aman R. Agrawal[1], Christian M. Pluchar[1], Anthony J. Brady[3], Zhen Liu[4], Quntao Zhuang[1,3,5], Dalziel J. Wilson[1] & Zheshen Zhang[1,2,3,6]

Optomechanical systems have been exploited in ultrasensitive measurements of force, acceleration and magnetic fields. The fundamental limits for optomechanical sensing have been extensively studied and now well understood—the intrinsic uncertainties of the bosonic optical and mechanical modes, together with backaction noise arising from interactions between the two, dictate the standard quantum limit. Advanced techniques based on non-classical probes, in situ ponderomotive squeezed light and backaction-evading measurements have been developed to overcome the standard quantum limit for individual optomechanical sensors. An alternative, conceptually simpler approach to enhance optomechanical sensing rests on joint measurements taken by multiple sensors. In this configuration, a pathway to overcome the fundamental limits in joint measurements has not been explored. Here we demonstrate that joint force measurements taken with entangled probes on multiple optomechanical sensors can improve the bandwidth in the thermal-noise-dominant regime or the sensitivity in the shot-noise-dominant regime. Moreover, we quantify the overall performance of entangled probes with the sensitivity–bandwidth product and observe a 25% increase compared with that of classical probes. The demonstrated entanglement-enhanced optomechanical sensors would enable new capabilities for inertial navigation, acoustic imaging and searches for new physics.

Optomechanical sensors[1,2] have garnered substantial interest owing to their high sensitivity in the measurements of force[3], acceleration[4] and magnetic fields[5]; immunity to electromagnetic interference; and a small footprint[3,4]. As extensively studied in the field of cavity optomechanics[6], the superior performance of optomechanical sensors stems from their low-noise readout mechanism based on the parametric coupling of an optical field and a mechanical oscillator. In cavity optomechanical sensors, a probe field is coupled into an optical cavity where a mechanical oscillator resides. Physical displacement of the mechanical oscillator shifts the cavity's resonant frequency, which, in turn, shifts the phase of the field leaving the cavity. The sensitivity of the displacement measurement is typically bounded by the standard quantum limit (SQL) dictated by two fundamental noise sources including imprecision noise, also known as the shot noise owing to the photon-number fluctuations in the probe, and backaction noise arising from the interaction between the radiation-pressure shot noise and the mechanical oscillator[7–9]. Several techniques have been developed in recent years to improve the sensitivity of individual optomechanical

---

[1]James C. Wyant College of Optical Sciences, University of Arizona, Tucson, AZ, USA. [2]Department of Materials Science and Engineering, University of Arizona, Tucson, AZ, USA. [3]Department of Electrical and Computer Engineering, University of Arizona, Tucson, AZ, USA. [4]School of Physics and Astronomy, University of Minnesota, Minneapolis, MN, USA. [5]Ming Hsieh Department of Electrical and Computer Engineering, University of Southern California, Los Angeles, CA, USA. [6]Department of Electrical Engineering and Computer Science, University of Michigan, Ann Arbor, MI, USA. e-mail: yixia.light@gmail.com; zszh@umich.edu

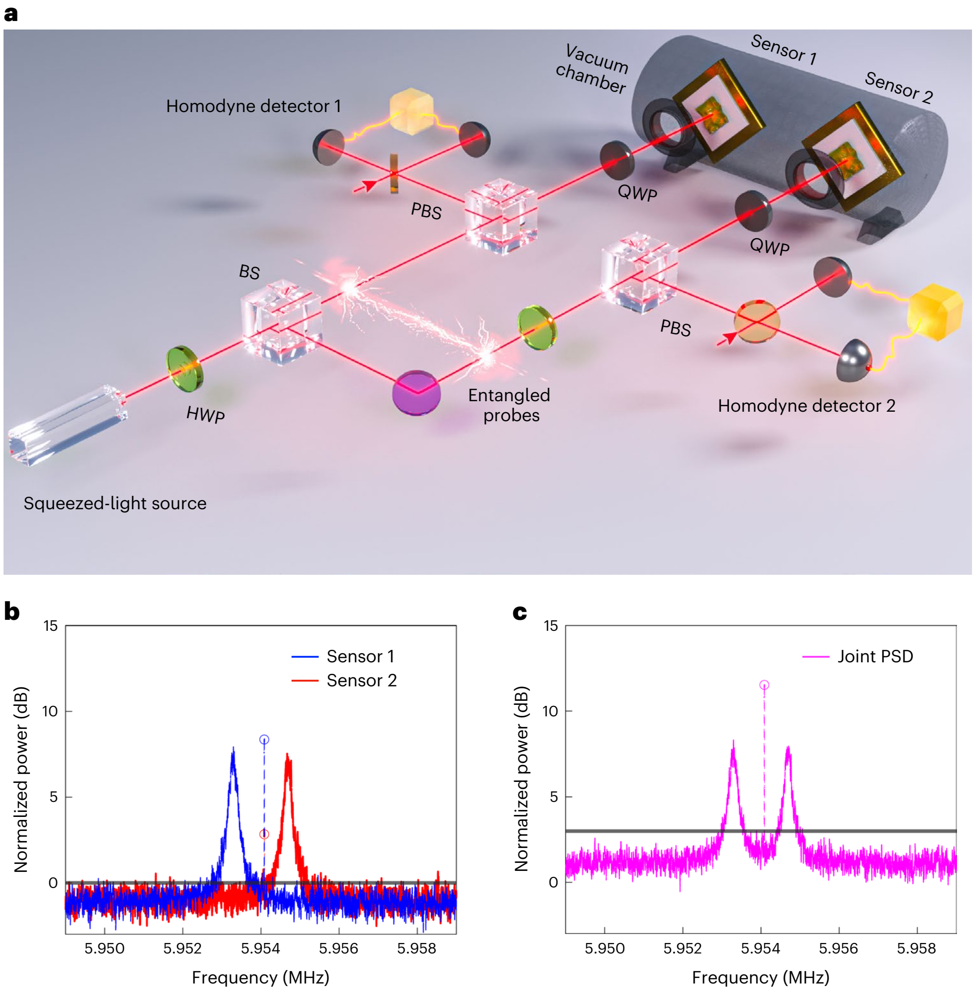

Fig. 1 | Experimental scheme and measurement power spectra. **a**, Experimental setup. BS, beamsplitter; PBS, polarizing beamsplitter; QWP, quarter-wave plate. **b**, Normalized PSDs of the individual homodyne measurement for the displacement of each membrane using entangled probes. Individual shot-noise PSD (grey line) is normalized to unity. **c**, Normalized PSD of joint homodyne measurement for the displacements of both membranes. Joint shot-noise PSD (grey line) is normalized to 3 dB. The circles mark the delta peaks. The resolution bandwidth is 10 Hz (Methods describe the measurements and data processing).

sensors. To combat imprecision noise, probes carrying squeezed light have been employed in advanced LIGO[10] and Virgo[11] detectors to enable a 3 dB sensitivity improvement, as well as in optomechanical magnetometry to enhance the sensitivity and bandwidth in detecting magnetic fields[12]. Alternatively, backaction-evading measurements, quantum non-demolition measurements and imprecision-backaction correlations provide a route to beating the SQL. These approaches have been implemented in cavity optomechanics using two-tone driving[13,14], negative-mass oscillators[15–17] and the intrinsic optomechanical Kerr nonlinearity[18–21].

Apart from these intriguing advances in optomechanical measurement techniques with a single sensor, a parallel route to enhance optomechanical measurements builds on increasing the number of sensors. Per the central limit theorem, averaging the measurement outcomes of M identical and independent sensors reduces the statistical uncertainty by a factor of $1/\sqrt{M}$. As such, a large number of sensors can boost the measurement sensitivity in detecting a common signal, a scenario pertinent to a wide range of sensing tasks from earthquake-warning systems[22] to dark-matter searches[23–27].

Quantum metrology harnesses non-classical resources, for example, entanglement[28,29], to outperform the $1/\sqrt{M}$ factor of joint measurements, also known as the SQL scaling[30]. Distributed quantum sensing is a quantum metrology paradigm that leverages entanglement shared by multiple sensors to achieve—in an ideal situation—a more favourable Heisenberg scaling of $1/M$ for the joint measurement sensitivity[31–34]. Recent distributed quantum sensing experiments have demonstrated that entangled sensors outperform separable sensors in estimating global parameters such as the average optical phase shifts[35–37] and radio-frequency phase gradients[38]. To date, entanglement-enhanced optomechanical sensing has not been explored, to the best of our knowledge. In this work, we take a critical step to surpass the SQL scaling for arrayed optomechanical sensors by verifying that entangled probes improve joint force measurements with two mechanical membranes. We observe that entangled probes reduce the joint noise floor by 2.0 ± 0.2 dB, leading to a 40% improvement in force sensitivity in the shot-noise-dominant regime. In addition, entangled probes also extend the frequency range over which thermal noise is dominant, thus enhancing the sensor bandwidth by 20%. We further quantify the joint sensitivity and bandwidth with respect to the resonant frequency difference. We assess the overall performance of joint force detection using the sensitivity–bandwidth product (SBP) as a figure of merit. Finally, we investigate joint force sensing of two incoherent forces, demonstrating that entangled probes can shorten the integration time by 60% (limited by 2 dB squeezing in the imprecision noise limit) and improve the sensing bandwidth by 20% in the thermal noise limit, accelerating the spectral scanning rate in searches for unknown signals.

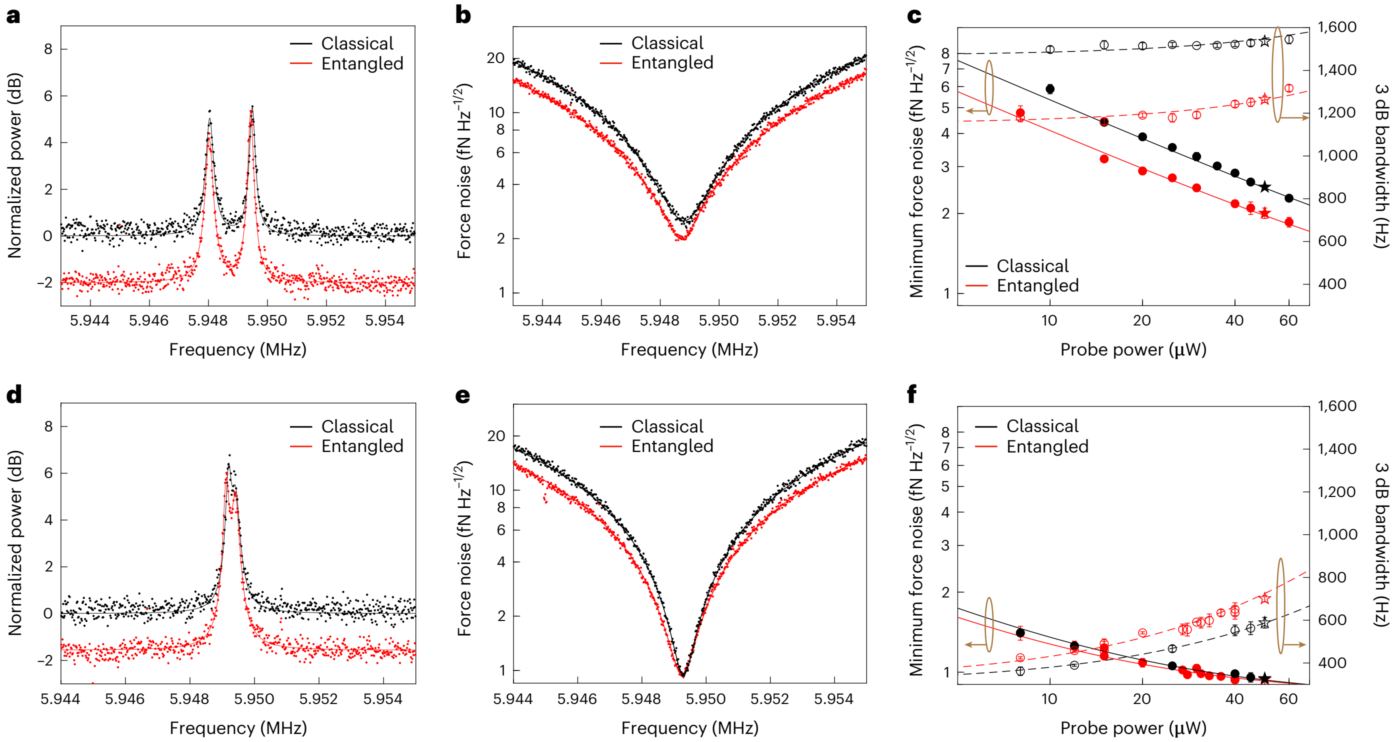

Fig. 2 | Entanglement-enhanced versus classical optomechanical sensing. **a**,**d**, Normalized joint PSDs of homodyne measurements for displacements. Joint shot noise is normalized to unity. **b**,**e**, Joint force noise at 50 μW probe power. **c**,**f**, Joint minimum force noise (solid lines) and bandwidth (dashed lines) at different probe power levels. Filled dots, minimum force noise; open dots, bandwidth; stars, fitted from force noise in **b** and **e**. Resonant frequency difference, 1,422 Hz (**a**–**c**) and 262 Hz (**d**–**f**). In all the figures, entangled probes are indicated in red; classical probes, black; experimental data, dots; theoretical data, curves. The error bars indicate systematic errors that account for drifting in frequency difference and optomechanical coupling. Statistical errors are negligible compared with systematic errors (Methods). The resolution bandwidth is 20 Hz.

Experimental implementation

The workhorse for entanglement-enhanced optomechanical sensing is squeezed light that is split into multiple arms to create entangled probes. The quantum advantage of this approach over separable classical probes stems from the correlated shot noise across the entangled probes, in the same vein as the recent entangled sensor network experiments[35,38]. Figure 1a sketches the experimental setup. The probes couple to two separate optomechanical sensors, each comprising a 100 × 100 μm^2 Si$_3$N$_4$ membrane with reflectively $R \approx 11.5\%$ atop a high-reflectivity ($R > 99.9\%$) mirror, forming an optical cavity with a finesse of ~3. Each membrane supports a set of high-Q drum modes with an effective mass of 6.75×10^{-13} kg at resonant frequencies of a few megahertz. We study sensing with the first higher-order mode of the two membranes at $\Omega_1/2\pi \approx 5.953$ MHz and $\Omega_2/2\pi \approx 5.955$ MHz, with damping rates of $\Gamma_1/2\pi \approx 200$ Hz and $\Gamma_2/2\pi \approx 260$ Hz. Homodyne measurements of the phase quadratures of the output probes from each cavity yield spectral amplitudes of

$$\hat{Y}^{(i)}_{\mathrm{out}}(\omega) = \hat{Y}^{(i)}_{\mathrm{in}}(\omega) + \alpha_i \beta_i \chi_i(\omega)\left[\hat{F}^{(i)}_{\mathrm{th}}(\omega) + \hat{F}^{(i)}_{\mathrm{sig}}(\omega)\right], \qquad (1)$$

where $i \in \{1, 2\}$ is the sensor index, $\hat{Y}^{(i)}_{\mathrm{in}}(\omega)$ is the phase quadrature of the input probe, α_i^2 is the mean photon number of each input probe (we assume α_i to be real for simplicity), $\beta_i = 4\sqrt{2G_i/\kappa_i}$ is the optomechanical transduction efficiency, G_i is the parametric coupling between the cavity's resonant frequency and mechanical oscillator position, κ_i is the cavity decay rate, $\chi_i(\omega) = \frac{1/m_{\mathrm{eff}}}{\Omega_i^2 - \omega^2 + \mathrm{i}\omega\Gamma_i}$ is the mechanical susceptibility, m_{eff} is the effective mass, $\hat{F}^{(i)}_{\mathrm{th}}(\omega)$ is the spectral amplitude of the thermal force and $\hat{F}^{(i)}_{\mathrm{sig}}(\omega)$ is the spectral amplitude of the force signal (backaction noise is negligible in our current system owing to the low cavity finesse). The estimation of the average force at the two sensors of nearly equal optomechanical transduction efficiencies ($\beta_1 \approx \beta_2 = \beta$) is carried out using near-optimal entangled probes generated by evenly splitting the squeezed light into two arms[35,38] ($\alpha_1 = \alpha_2 = \alpha_c/\sqrt{2}$), where α_c^2 is the mean photon number at the carrier wavelength of squeezed light. To achieve optimal performance, the frequency-dependent entangled state needs to be engineered according to the force transduction efficiencies at each sensor over the entire sensing bandwidth (Supplementary Section IC), similar to frequency-dependent squeezed light[39,40]. The impacts of loss and detector inefficiency are accounted for in the first term of equation (1) (Supplementary Section IB).

Results

To capture the physics behind entanglement-enhanced optomechanical sensing, we plot the power spectral densities (PSDs), namely, $S_{Y^{(1)}_{\mathrm{out}}Y^{(1)}_{\mathrm{out}}}(\omega)$ (blue) and $S_{Y^{(2)}_{\mathrm{out}}Y^{(2)}_{\mathrm{out}}}(\omega)$ (red), of the homodyne measurements for membrane displacements (Fig. 1b) normalized to the shot-noise level (SNL) represented by the grey line at unity (Supplementary Section I provides the definition of the PSD). The imprecision noise floor of each sensor is ~1 dB below the SNL, whereas the measured squeezing level from the source is ~4 dB below the SNL[38] (Supplementary Section III provides the loss contributions). The spectra also show a thermal-noise-dominant band in the vicinity of the mechanical resonant frequencies, manifested as two broad peaks. The radiation-pressure test forces on the membranes are created by an auxiliary amplitude-modulated 775 nm laser, yielding two delta peaks that are 2.80 and 8.36 dB above the SNL (Fig. 1b, circles). The signal-to-noise

https://doi.org/10.1038/s41566-023-01178-0

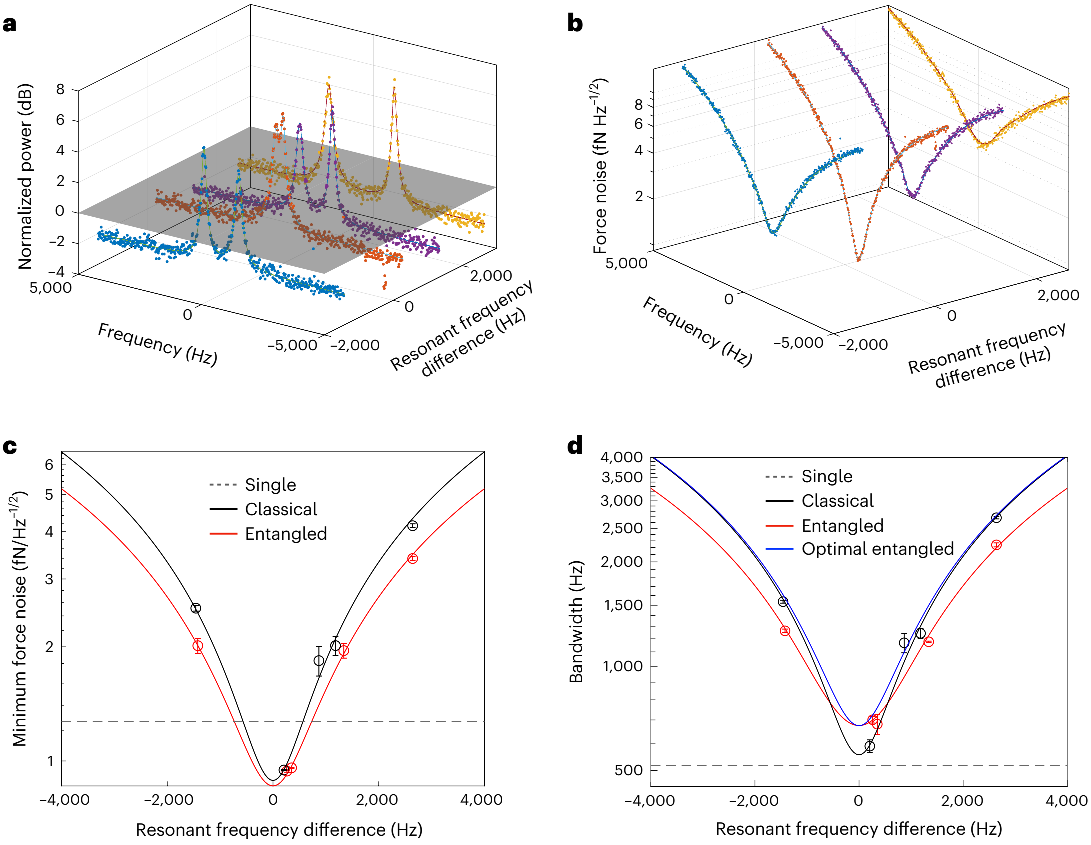

Fig. 3 | Sensitivity and bandwidth reconfigured by resonant frequency difference. a,**b**, Normalized PSD of joint homodyne measurement (**a**) and joint force sensitivities based on entangled probes at 50 μW power (**b**). The blue, red, purple and yellow curves correspond to resonant frequency differences of −1,422, 262, 1,339 and 2,641 Hz. Shaded plane, SNL. **c**,**d**, Sensitivity (**c**) and bandwidth $\mathcal{B}_{3\mathrm{dB}}/2\pi$ (**d**) at various resonant frequency differences for entangled (red), classical (black) and optimal entangled (blue) probes with 50 μW power. Circles, experimental data; solid lines, theoretical data; dashed lines, single classical sensor. The error bars indicate systematic errors that account for drifting in frequency difference and optomechanical coupling. Statistical errors are negligible compared with systematic errors (Methods).

ratio at each sensor is slightly improved due to the residue single-mode squeezing in each probe. Figure 1c draws the joint homodyne PSD $S_{Y^{(\mathrm{joint})}_{\mathrm{out}}Y^{(\mathrm{joint})}_{\mathrm{out}}}$ obtained by adding the homodyne measurement records from both sensors, showing a more substantial signal-to-noise ratio advantage for the entangled probes. The signals coherently add to 11.5 dB, whereas the joint imprecision noise floor increases to 1.0 dB for entangled probes, compared with the anticipated 3.0 dB for classical probes. Notably, this 2 dB noise reduction implies a joint sensitivity improvement beyond the $1/\sqrt{M}$ SQL scaling—beneficial for broadband, shot-noise-limited distributed force-sensing applications, such as accelerometer arrays.

Entanglement-enhanced measurement sensitivity

We next investigate the performance of average force estimation $\bar{F}=(F^{(1)}+F^{(2)})/2$ based on entangled or classical probes interrogating two mechanical sensors with a large resonant frequency difference (1,422 Hz). Figure 2a shows the joint homodyne PSDs for the two cases with the joint SNL normalized to unity. The noise peaks in the vicinity of the mechanical resonant frequencies are of equal magnitude for the entangled and classical probes due to the dominant thermal noise in this region. Nonetheless, the entangled probes reduce the off-resonant imprecision noise floor from the SNL by 2 dB. To characterize the advantage this offers to force sensing, Fig. 2b shows the joint force noise $\sqrt{S_{\bar{F}\bar{F}}}$ derived by rescaling the individual output-phase quadratures: $\hat{F}^{(i)}=\hat{Y}^{(i)}_{\mathrm{out}}(\omega)/(\alpha_i\beta_i|\chi_i(\omega)|)$ and adding them together (Supplementary Section I). The minimum force-noise PSDs $S_{\bar{F}_{\mathrm{min}}\bar{F}_{\mathrm{min}}}$ associated with the classical probes (Fig. 2, black) is achieved at $\omega_{\mathrm{min}}=\frac{1}{2}\sqrt{-\Gamma_1^2-\Gamma_2^2+2(\Omega_1^2+\Omega_2^2)}\approx\frac{\Omega_1+\Omega_2}{2}\equiv\bar{\Omega}$ in the shot-noise-dominant region between the two resonant frequencies. The two mechanical susceptibilities coincide near $\bar{\Omega}$ as $|\chi_1(\bar{\Omega})|=|\chi_2(\bar{\Omega})|$. The entangled probes (Fig. 2, red) reduce the force noise by 20%. In Fig. 2c, we plot the minimum force noise $\sqrt{S_{\bar{F}_{\mathrm{min}}\bar{F}_{\mathrm{min}}}}$ (filled dots) for the entangled (red) and classical (black) probes at different power levels and the solid lines denote theoretical predictions. The minimum force-noise PSD is approximated by

$$S_{\bar{F}_{\mathrm{min}}\bar{F}_{\mathrm{min}}}\approx\frac{m_{\mathrm{eff}}^2}{\beta^2\alpha_{\mathrm{c}}^2}\bar{\Omega}^2(\bar{\Gamma}^2+\Delta\Omega^2)S_{Y_0Y_0}+S_{\bar{F}_{\mathrm{th}}\bar{F}_{\mathrm{th}}} \qquad (2)$$

in the limit of $|\Omega_1-\Omega_2|$ and $\Gamma_1,\Gamma_2\ll\Omega_1,\Omega_2$, where $S_{Y_0Y_0}=V/2$ with $V=1.00$ for coherent states and $V\approx0.63$ for the entangled state with the measured 2 dB squeezing and $\bar{\Gamma}=\sqrt{(\Gamma_1^2+\Gamma_2^2)/2}$. Here $\Delta\Omega=\Omega_1-\Omega_2$ is the resonant frequency difference. The minimum force noise scales as $1/\alpha_{\mathrm{c}}$ until thermal noise becomes comparable with imprecision noise. We define the peak sensitivity as $\mathcal{S}=1/S_{\bar{F}_{\mathrm{min}}\bar{F}_{\mathrm{min}}}$. The entangled probes offer an improvement in sensitivity by reducing the imprecision noise floor below the SNL by 2 dB.

In Fig. 2d, we plot the joint homodyne PSDs of two sensors with a small resonant frequency difference (262 Hz) interrogated by entangled (red) or classical (black) probes, each with

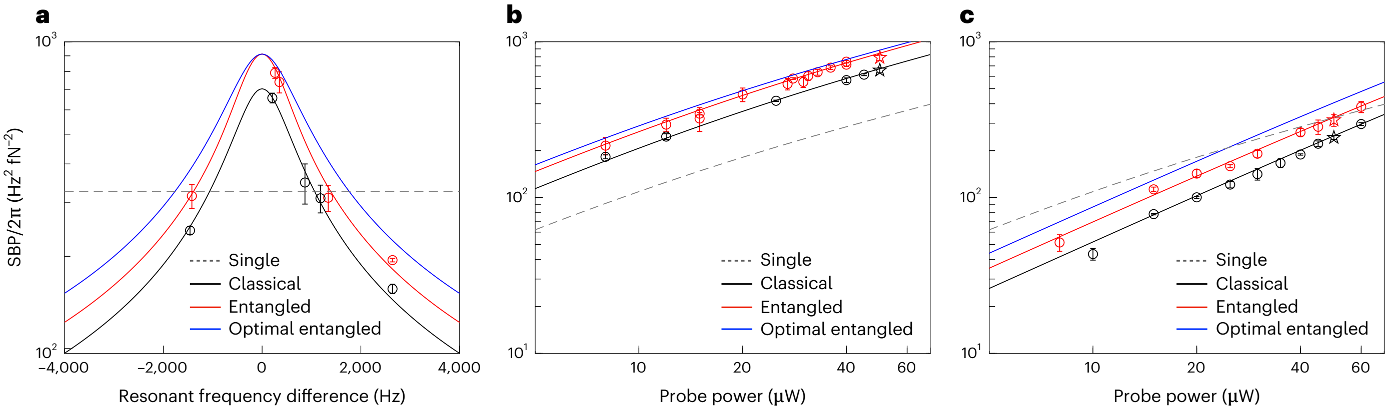

Fig. 4 | Sensitivity-bandwidth product as a figure of merit for joint force measurements. a, Sensitivity-bandwidth product (SBP) versus frequency difference. Probe power is 50 μW for all the measurements. **b**,**c**, SBP versus probe power at resonant frequency difference of 262 Hz (**b**) and 1,422 Hz (**c**). For all the figures, entangled probes are denoted by red; classical probes, black; optimal entangled probes, blue; experimental data, dots; theory, solid lines; single classical sensor, dashed lines. The error bars indicate systematic errors that account for drift in resonant frequency difference and optomechanical coupling. Statistical errors are negligible compared with systematic errors (Methods).

50 μW power. Figure 2e shows that the dominant thermal noise $\sqrt{S_{\bar{F}_{\rm th}\bar{F}_{\rm th}}} = \sqrt{\left(S_{F_{\rm th}^{(1)}F_{\rm th}^{(1)}} + S_{F_{\rm th}^{(2)}F_{\rm th}^{(2)}}\right)/2}$ around the resonant frequencies limits the peak force sensitivity for the joint force measurements with entangled and classical probes, where $\sqrt{S_{F_{\rm th}^{(i)}F_{\rm th}^{(i)}}} = \sqrt{2\Gamma_i m_{\rm eff} k_{\rm B} T} \approx 10^{-15}$ N Hz$^{-1/2}$ is the thermal noise at each sensor. Figure 2f shows the minimum force noise (filled dots) at different probe power levels. The sensitivities for both entangled and classical probes converge to the thermal noise limit as the probe power increases. However, the entangled probes can improve the sensing bandwidth, as elaborated later.

Entanglement-enhanced measurement bandwidth

The response of a mechanical oscillator to external stimuli is enhanced by its quality (Q) factor, which boosts the transduction efficiency around the resonant frequency. Due to coupling to the thermal bath, the force sensitivity of a single sensor is limited by the thermal noise that inversely scales as the Q-to-mass ratio. Recent developments in ultrahigh-Q mechanical resonators has enabled dramatic improvements in force sensitivity at the cost of a narrow sensitivity bandwidth[41–45]. By contrast, joint measurements undertaken by M identical mechanical sensors with homogeneous resonant frequencies can improve force sensitivity by the SQL scaling of $1/\sqrt{M}$ and maintain a bandwidth similar to that of a single sensor. Entangled probes can, moreover, increase the sensing bandwidth of sensor arrays, in analogy to recent demonstrations of squeezed-light-enhanced bandwidths for a microwave cavity sensor[46,47] and an optomechanical magnetometer[12].

As shown in Fig. 2e, it is evident that the bandwidth for entangled probes (red) is broadened compared with that for classical probes (black). To quantify the bandwidth improvement by entangled probes, we define the 3 dB sensing bandwidth as $\mathcal{B}_{3\rm dB} \equiv \omega_{3\rm dB+} - \omega_{3\rm dB-}$, the width of the frequency band over which the force noise power is within a factor of 2 of the minimum, that is, $S_{\bar{F}\bar{F}}(\omega_{3\rm dB\pm}) = 2S_{\bar{F}_{\rm min}\bar{F}_{\rm min}}$. Figure 2f shows the 3 dB sensing bandwidths (open dots) at different probe power levels and the dashed lines correspond to theoretical predictions. The bandwidth approximately scales as $\alpha_{\rm c}$ in the thermal-noise-dominated regime and the entangled probes maintain a 20% sensing bandwidth improvement. At large resonant frequency differences (Fig. 2c), the bandwidth is predominantly determined by the resonant frequency difference (1,422 Hz) and marginally increases with the probe power. The bandwidth for the entangled probes is worse than that of the classical probes because the entangled state around the resonant frequencies is not optimized to account for the large disparity in mechanical transduction efficiencies of the two sensors. Frequency-dependent entangled states are required to fully exploit the advantage of quantum correlations.

Sensitivity-bandwidth product

The previous two sets of data illustrate that sensors with a large resonant frequency difference enjoy a larger measurement bandwidth, and their sensitivity minimum can be enhanced by entangled probes. Conversely, sensors with a small resonant frequency difference possess higher sensitivity, whereas entangled probes can increase the measurement bandwidth. To highlight this feature, we first display (Fig. 3a) the homodyne PSDs acquired by entangled probes with 50 μW power at four resonant frequency differences. Figure 3b then visualizes the dependence of force noise and bandwidth on the resonant frequency difference. Figure 3c,d depicts the minimum force noise and 3 dB bandwidths associated with the entangled (red lines) and classical (black lines) probes at different frequency differences, showing good agreement between theory and experiment. The bandwidth with entangled light approaches the performance of the optimal entangled state (Fig. 3d, blue line) near the zero resonant frequency difference but drops below the bandwidth of both optimal entangled and classical light at large resonant frequency differences, whereas the minimum force noise using entangled light coincides with the minimum force noise achieved by the optimal entangled state. As a comparison, we also show the theoretical minimum force noise and 3 dB bandwidth of a single sensor (Fig. 3c,d, dashed grey lines) probed with classical light. The minimum force noise for the two sensors with similar resonant frequencies is reduced by about $1/\sqrt{2}$ compared with that of a single sensor. However, the peak sensitivity of two sensors with a large resonant frequency difference is worse than that of a single sensor as joint imprecision noise is dominant over thermal noise. The bandwidth of two sensors, however, is always larger than that of a single sensor and increases with the resonant frequency difference.

For broadband sensing, high sensitivity over a wide frequency range is desirable. Following another work[48], we adopt the SBP as a figure of merit to assess the performance of the joint force measurement. This metric—similar to integrated sensitivity[49]—has been shown to be a useful figure of merit for broadband sensing applications[47]. The SBPs of the classical and optimal entangled state are given by (equation (S40) in Supplementary Section IE)

https://doi.org/10.1038/s41566-023-01178-0

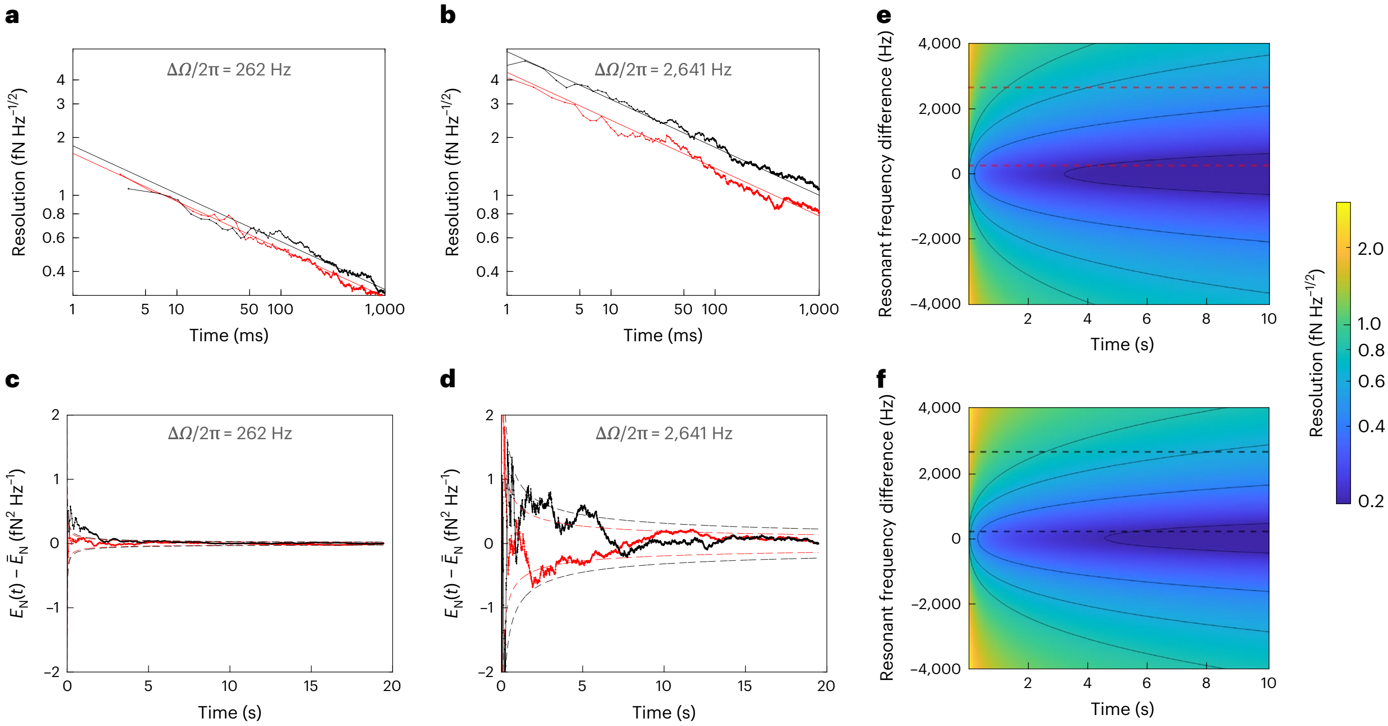

Fig. 5 | Incoherent force sensing. a,**b**, Force resolution versus integration time based on 50 μW entangled (red) and classical (black) probes on sensors with a resonant frequency difference of 262 Hz (**a**) and 2,641 Hz (**b**). **c**,**d**, Estimate of force-noise power at different times for 50 μW entangled (red) and classical (black) probes for resonant frequency difference of 262 Hz (**c**) and 2,641 Hz (**d**). The dashed lines derived from the force resolution in **a** and **b** are the bounds for force-noise power. **e**,**f**, Simulated force resolution versus resonant frequency difference and time for entangled (**e**) and classical (**f**) probes. Theory lines in **a** and **b** are marked as the dashed lines in **e** and **f**. The black solid lines are the contours of resolution at {0.21, 0.41, 0.61, 0.81} fN Hz$^{-1/2}$.

$$\mathcal{S} \times \mathcal{B}_{3\mathrm{dB}} \approx \frac{\beta\alpha_{\mathrm{c}}}{\omega_{\min} m_{\mathrm{eff}}\sqrt{S_{Y_0Y_0}}}\sqrt{\frac{1}{S_{\bar{F}_{\min}\bar{F}_{\min}}}}. \qquad (3)$$

The SBP of the entangled probe in our experiment is suboptimal and lies in between the ones for the classical and optimal entangled probes. Figure 4a shows the SBP at various resonant frequency differences for the classical (black), entangled (red) and optimal entangled (blue) probes. The probe power is fixed at around 50 μW at each sensor for both classical and entangled probes. SBPs decrease with respect to the resonant frequency difference, as expected from equation (3), according to which the joint imprecision noise increases with resonant frequency differences. We also plot the SBP for a classical single sensor (Fig. 4, dashed line) probed with 50 μW as a comparison. Beyond certain resonant frequency differences, the SBP for entangled probes can even drop below that of a single sensor. In the small resonant frequency difference scenario, the SBP of the entangled probes in our experiment is on par with that of the optimal entangled probes, surpassing the SBP of classical probes by a factor of $1/\sqrt{V} \approx 1.25$. We plot the SBPs against different probe power levels at two resonant frequency differences of 262 and 1,422 Hz (Fig. 4b,c). The SBPs of two sensors increase with respect to the square root of the mean photon number α_{c} in the thermal-noise-dominant regime (Fig. 4b) and the mean photon number α_{c}^2 in the imprecision-noise-dominant regime (Fig. 4c).

Entanglement-enhanced incoherent force sensing

Optomechanical sensors have been exploited in detecting weak incoherent forces embedded in a thermal noise background[3,50], a regime pertinent to dark-matter searches[23,49]. Joint measurements taken by multiple sensors can increase the signal-to-noise ratio by lowering the measurement noise, thereby enhancing the resolution in incoherent force sensing. Entangled probes, in this regard, can further improve incoherent force sensing by increasing the measurement bandwidth (resolution) in the thermal-noise-dominant (imprecision-noise-dominant) scenario. Following other work[3,50], we choose the energy estimator as a performance metric and use it to demonstrate a quantum advantage in the measurement of uncorrelated, incoherent forces.

We define the equivalent force spectral resolution (EFSR) as $\delta F_{\mathrm{N}} = \sqrt{\delta E_{\mathrm{N}}(t)}$, that is, the square root of the standard deviation of the overall force noise within its 3 dB bandwidth, which includes the thermal force and an equivalent force noise contributed by the imprecision noise of the probes, where $E_{\mathrm{N}}(t) = \int_0^t \mathrm{d}tF_{\mathrm{N}}(t)^2/t$ is the noise-force energy averaged over t seconds. An incoherent force is detectable only if the EFSR is finer than its standard deviation. Figure 5a shows the EFSR versus integration time for the entangled (red) and classical (black) probes, each carrying 50 μW of power. The resonant frequency difference is 262 Hz; therefore, the measurement is dominated by thermal noise, resulting in similar force resolutions for the entangled and classical probes. The data corroborate the force resolution scaling of $t^{-1/4}$ for both types of probe, as predicted by theory[3]. However, the entangled probes offer a larger measurement bandwidth (enabling accelerated search for unknown signals, in the same spirit of squeezed-light-enhanced dark-matter search based on microwave cavity sensors[46,47]). Figure 5b shows the time dependence of the force resolution for sensors with a 2,641 Hz resonant frequency difference. The entangled probes reduce the integration time by 60% over that of the classical probes in arriving at the same force resolution. Figure 5e,f presents the simulation result for the force resolution versus the resonant frequency difference and integration time attained by entangled and classical probes. The dashed lines (Fig. 5e,f) correspond to the theory curves in Fig. 5a,b. The estimated force power $(E_{\mathrm{N}}(t) - \bar{E}_{\mathrm{N}})$ is shown in Fig. 5c,d and it converges to zero at a long integration time, where $\bar{E}_{\mathrm{N}}$ is the mean noise-force power. The dashed lines also correspond to the force resolution in Fig. 5a,b. A stationary incoherent force signal can only be resolved when its energy within the detection bandwidth exceeds the noise power uncertainty at a given averaging time. Without loss of generality, we only plot the estimate for the total noise force. An example of the signal–force estimate is presented in Supplementary Section IIIE.

Discussion and conclusions

The gain in measurement sensitivity with two entangled probes compared with a single measurement supplied with the same amount of squeezing at the source is a factor of $\sqrt{2}$. Our approach can be readily scaled up to more optomechanical sensors by leveraging multimode entangled probes[33] created by splitting a single-mode squeezed state through a linear optical network. It should be noted that the vacuum noise injected from the input ports of the beamsplitters does not contribute to the joint measurement as it is eliminated in post-processing[33]. The force sensitivity of our experiment is limited by the thermal noise near resonance and imprecision noise off-resonance, a regime pertinent to many optomechanical sensing applications including inertial sensing[4,51], thermal sensing[52] and distributed acoustic sensing[53–55]. Cryogenic cooling and increasing the probe power would enhance the sensor performance. Yet, the entangled probes always enjoy quantum advantages over classical laser light subject to the same level of probe power. In practice, our entanglement-based approach can mitigate photodamage in bioimaging[56] as well as the photothermal effect and radiation pressure instability in optomechanical sensing[57,58]. It is worth noting that the entangled probes can also enhance the sensitivity at the displacement SQL, where imprecision and backaction noise equally contribute at mechanical resonance. A full analysis of the role of backaction in entanglement-enhanced optomechanical sensing is presented elsewhere[49]. The SBP (equation (3)) serves as a figure of merit for the sensors. One can, in general, define an SBP built on a different core function tailored to target signals with a known non-trivial spectrum or with a frequency-dependent coupling strength (for example, quantum chromodynamics axions[59]) without the loss of entanglement-enabled enhancement. Also, note that another work[60] defined a quantity analogous to SBP to study the sensitivity–bandwidth tradeoff (Supplementary Section IE).

In conclusion, we have experimentally demonstrated entanglement-enhanced joint force measurements with two optomechanical sensors. Sensitivity and bandwidth enhancement enabled by entangled probes are predicted and observed. Specifically, optomechanical sensors jointly probed by entangled light generated from a passive beamsplitter array with squeezed-light input outperform the same sensors probed by classical laser light in force resolution and measurement bandwidth. Our work opens a new avenue for ultraprecise measurements with an array of quantum-enhanced sensors for applications ranging from inertial navigation[61] to acoustic sensing[62], as well as searches for new physics[47].

Online content

Any methods, additional references, Nature Portfolio reporting summaries, source data, extended data, supplementary information, acknowledgements, peer review information; details of author contributions and competing interests; and statements of data and code availability are available at https://doi.org/10.1038/s41566-023-01178-0.

References

1. Li, B.-B., Ou, L., Lei, Y. & Liu, Y.-C. Cavity optomechanical sensing. *Nanophotonics* **10**, 2799–2832 (2021).
2. Liu, X. et al. Progress of optomechanical micro/nano sensors: a review. *Int. J. Optomechatronics* **15**, 120–159 (2021).
3. Gavartin, E., Verlot, P. & Kippenberg, T. J. A hybrid on-chip optomechanical transducer for ultrasensitive force measurements. *Nat. Nanotechnol.* **7**, 509–514 (2012).
4. Krause, A. G., Winger, M., Blasius, T. D., Lin, Q. & Painter, O. A high-resolution microchip optomechanical accelerometer. *Nat. Photon.* **6**, 768–772 (2012).
5. Forstner, S. et al. Cavity optomechanical magnetometer. *Phys. Rev. Lett.* **108**, 120801 (2012).
6. Aspelmeyer, M., Kippenberg, T. J. & Marquardt, F. Cavity optomechanics. *Rev. Mod. Phys.* **86**, 1391 (2014).
7. Caves, C. M., Thorne, K. S., Drever, R. W., Sandberg, V. D. & Zimmermann, M. On the measurement of a weak classical force coupled to a quantum-mechanical oscillator. I. Issues of principle. *Rev. Mod. Phys.* **52**, 341 (1980).
8. Clerk, A. A., Devoret, M. H., Girvin, S. M., Marquardt, F. & Schoelkopf, R. J. Introduction to quantum noise, measurement, and amplification. *Rev. Mod. Phys.* **82**, 1155 (2010).
9. Teufel, J. D., Donner, T., Castellanos-Beltran, M., Harlow, J. W. & Lehnert, K. W. Nanomechanical motion measured with an imprecision below that at the standard quantum limit. *Nat. Nanotechnol.* **4**, 820–823 (2009).
10. Tse, M. E. et al. Quantum-enhanced advanced LIGO detectors in the era of gravitational-wave astronomy. *Phys. Rev. Lett.* **123**, 231107 (2019).
11. Acernese, F. et al. Increasing the astrophysical reach of the advanced Virgo detector via the application of squeezed vacuum states of light. *Phys. Rev. Lett.* **123**, 231108 (2019).
12. Li, B.-B. et al. Quantum enhanced optomechanical magnetometry. *Optica* **5**, 850–856 (2018).
13. Shomroni, I., Qiu, L., Malz, D., Nunnenkamp, A. & Kippenberg, T. J. Optical backaction-evading measurement of a mechanical oscillator. *Nat. Commun.* **10**, 2086 (2019).
14. Ockeloen-Korppi, C. et al. Quantum backaction evading measurement of collective mechanical modes. *Phys. Rev. Lett.* **117**, 140401 (2016).
15. Tsang, M. & Caves, C. M. Evading quantum mechanics: engineering a classical subsystem within a quantum environment. *Phys. Rev. X* **2**, 031016 (2012).
16. Mercier de Lépinay, L., Ockeloen-Korppi, C. F., Woolley, M. J. & Sillanpää, M. A. Quantum mechanics–free subsystem with mechanical oscillators. *Science* **372**, 625–629 (2021).
17. Møller, C. B. et al. Quantum back-action-evading measurement of motion in a negative mass reference frame. *Nature* **547**, 191–195 (2017).
18. Mason, D., Chen, J., Rossi, M., Tsaturyan, Y. & Schliesser, A. Continuous force and displacement measurement below the standard quantum limit. *Nat. Phys.* **15**, 745–749 (2019).
19. Sudhir, V. et al. Quantum correlations of light from a room-temperature mechanical oscillator. *Phys. Rev. X* **7**, 031055 (2017).
20. Purdy, T., Grutter, K., Srinivasan, K. & Taylor, J. Quantum correlations from a room-temperature optomechanical cavity. *Science* **356**, 1265–1268 (2017).
21. Kampel, N. et al. Improving broadband displacement detection with quantum correlations. *Phys. Rev. X* **7**, 021008 (2017).
22. D'Alessandro, A., Scudero, S. & Vitale, G. A review of the capacitive MEMS for seismology. *Sensors* **19**, 3093 (2019).
23. Carney, D., Hook, A., Liu, Z., Taylor, J. M. & Zhao, Y. Ultralight dark matter detection with mechanical quantum sensors. *New J. Phys.* **23**, 023041 (2021).
24. Brady, A. J. et al. Entangled sensor-networks for dark-matter searches. *PRX Quantum* **3**, 030333 (2022).
25. Derevianko, A. Detecting dark-matter waves with a network of precision-measurement tools. *Phys. Rev. A* **97**, 042506 (2018).
26. Carney, D. et al. Mechanical quantum sensing in the search for dark matter. *Quantum Sci. Technol.* **6**, 024002 (2021).

27. Carney, D., Ghosh, S., Krnjaic, G. & Taylor, J. M. Proposal for gravitational direct detection of dark matter. *Phys. Rev. D* **102**, 072003 (2020).
28. Gessner, M., Pezzè, L. & Smerzi, A. Sensitivity bounds for multiparameter quantum metrology. *Phys. Rev. Lett.* **121**, 130503 (2018).
29. Rudolph, H., Delić, U., Aspelmeyer, M., Hornberger, K. & Stickler, B. A. Force-gradient sensing and entanglement via feedback cooling of interacting nanoparticles. *Phys. Rev. Lett.* **129**, 193602 (2022).
30. Giovannetti, V., Lloyd, S. & Maccone, L. Quantum metrology. *Phys. Rev. Lett.* **96**, 010401 (2006).
31. Proctor, T. J., Knott, P. A. & Dunningham, J. A. Multiparameter estimation in networked quantum sensors. *Phys. Rev. Lett.* **120**, 080501 (2018).
32. Zhang, Z. & Zhuang, Q. Distributed quantum sensing. *Quantum Sci. Technol.* **6**, 043001 (2021).
33. Zhuang, Q., Zhang, Z. & Shapiro, J. H. Distributed quantum sensing using continuous-variable multipartite entanglement. *Phys. Rev. A* **97**, 032329 (2018).
34. Ge, W., Jacobs, K., Eldredge, Z., Gorshkov, A. V. & Foss-Feig, M. Distributed quantum metrology with linear networks and separable inputs. *Phys. Rev. Lett.* **121**, 043604 (2018).
35. Guo, X. et al. Distributed quantum sensing in a continuous-variable entangled network. *Nat. Phys.* **16**, 281–284 (2020).
36. Liu, L.-Z. et al. Distributed quantum phase estimation with entangled photons. *Nat. Photon.* **15**, 137–142 (2021).
37. Hong, S. et al. Quantum enhanced multiple-phase estimation with multi-mode *N00N* states. *Nat. Commun.* **12**, 5211 (2021).
38. Xia, Y. et al. Demonstration of a reconfigurable entangled radio-frequency photonic sensor network. *Phys. Rev. Lett.* **124**, 150502 (2020).
39. Kimble, H. J., Levin, Y., Matsko, A. B., Thorne, K. S. & Vyatchanin, S. P. Conversion of conventional gravitational-wave interferometers into quantum nondemolition interferometers by modifying their input and/or output optics. *Phys. Rev. D* **65**, 022002 (2001).
40. Zhao, Y. et al. Frequency-dependent squeezed vacuum source for broadband quantum noise reduction in advanced gravitational-wave detectors. *Phys. Rev. Lett.* **124**, 171101 (2020).
41. Ghadimi, A. H. et al. Elastic strain engineering for ultralow mechanical dissipation. *Science* **360**, 764–768 (2018).
42. Beccari, A. et al. Strained crystalline nanomechanical resonators with quality factors above 10 billion. *Nat. Phys.* **18**, 436–441 (2022).
43. MacCabe, G. S. et al. Nano-acoustic resonator with ultralong phonon lifetime. *Science* **370**, 840–843 (2020).
44. Tsaturyan, Y., Barg, A., Polzik, E. S. & Schliesser, A. Ultracoherent nanomechanical resonators via soft clamping and dissipation dilution. *Nat. Nanotechnol.* **12**, 776–783 (2017).
45. Høj, D. et al. Ultra-coherent nanomechanical resonators based on inverse design. *Nat. Commun.* **12**, 5766 (2021).
46. Malnou, M. et al. Squeezed vacuum used to accelerate the search for a weak classical signal. *Phys. Rev. X* **9**, 021023 (2019).
47. Backes, K. M. et al. A quantum enhanced search for dark matter axions. *Nature* **590**, 238–242 (2021).
48. Korobko, M. et al. Beating the standard sensitivity-bandwidth limit of cavity-enhanced interferometers with internal squeezed-light generation. *Phys. Rev. Lett.* **118**, 143601 (2017).
49. Brady, A. J. et al. Entanglement-enhanced optomechanical sensor array for dark matter searches. Preprint at *arXiv* https://doi.org/10.48550/arXiv.2210.07291 (2022).
50. Harris, G. I., McAuslan, D. L., Stace, T. M., Doherty, A. C. & Bowen, W. P. Minimum requirements for feedback enhanced force sensing. *Phys. Rev. Lett.* **111**, 103603 (2013).
51. Chowdhury, M. D., Agrawal A. R. & Wilson D. J. Membrane-based optomechanical accelerometry. *Phys. Rev. Applied* **19**, 024011 (2023).
52. Liu, S. et al. Room-temperature fiber tip nanoscale optomechanical bolometer. *ACS Photonics* **9**, 1586–1593 (2022).
53. Jousset, P. et al. Fibre optic distributed acoustic sensing of volcanic events. *Nat. Commun.* **13**, 1753 (2022).
54. Sladen, A. et al. Distributed sensing of earthquakes and ocean-solid Earth interactions on seafloor telecom cables. *Nat. Commun.* **10**, 5777 (2019).
55. Walter, F. et al. Distributed acoustic sensing of microseismic sources and wave propagation in glaciated terrain. *Nat. Commun.* **11**, 2436 (2020).
56. Casacio, C. A. et al. Quantum-enhanced nonlinear microscopy. *Nature* **594**, 201–206 (2021).
57. Rokhsari, H., Kippenberg, T. J., Carmon, T. & Vahala, K. J. Radiation-pressure-driven micro-mechanical oscillator. *Opt. Express* **13**, 5293–5301 (2005).
58. Arcizet, O., Cohadon, P.-F., Briant, T., Pinard, M. & Heidmann, A. Radiation-pressure cooling and optomechanical instability of a micromirror. *Nature* **444**, 71–74 (2006).
59. Hook, A. TASI lectures on the strong CP problem and axions. Preprint at *arXiv* https://doi.org/10.48550/arXiv.1812.02669 (2018).
60. Haghighi, I. M., Malossi, N., Natali, R., Di Giuseppe, G. & Vitali, D. Sensitivity-bandwidth limit in a multimode optoelectromechanical transducer. *Phys. Rev. Appl.* **9**, 034031 (2018).
61. Hines, A., Richardson, L., Wisniewski, H. & Guzman, F. Optomechanical inertial sensors. *Appl. Opt.* **59**, G167–G174 (2020).
62. Westerveld, W. J. et al. Sensitive, small, broadband and scalable optomechanical ultrasound sensor in silicon photonics. *Nat. Photon.* **15**, 341–345 (2021).

Methods

Squeezed-light source

Squeezed light at 1,550 nm is generated by pumping an optical parametrical amplifier cavity below the threshold. The pump light at 775 nm is phase locked to amplify the seed laser at 1,550 nm through a type-0 periodically poled $\mathrm{KTiOPO_4}$ nonlinear crystal embedded in an optical cavity. The output power of the squeezed light can be effectively tuned by adjusting the seed laser power. All the cavity lengths are locked based on the Pound–Drever–Hall technique using 24 MHz sidebands created by phase modulating the 1,550 nm pump laser. A measured squeezing spectrum is shown in Supplementary Fig. 2.

Calibration of optomechanical sensors

To measure the membrane displacement, the probe light is first converted into circular polarization by a quarter-wave plate and then focused onto the membrane. The displacement is encoded on the phase of the reflected probe, which is then separated by the same quarter-wave plate and polarizing beamsplitter. The phase quadrature is subsequently measured by a homodyne detector. The propagation loss from the optomechanical sensors to the detectors is measured to be around 18%. The interference visibility of homodyne measurement is optimized to 92%. The d.c. signal of the photocurrent is used to lock the phase between the local oscillator and probe light. The a.c. component of the photocurrent is sampled by a fast Fourier transform (FFT) spectrum analyser. The measured PSDs are fitted using equation (1) to extract the optomechanical coupling efficiency β and mechanical susceptibility $\chi(\omega)$.

Joint measurement of two optomechanical sensors with entangled probe light

We balance the optomechanical coupling efficiencies at the two sensors by slightly displacing the position of the light spot on one membrane. With identical coupling efficiencies, near-optimum entangled probes can be generated via splitting the squeezed light evenly into two arms so that each sensor receives 50% of the squeezed light. The disparity in resonant frequencies between the fabricated membranes can be as large as 300 kHz. We pick two membranes with similar resonant frequencies with a difference close to the linewidth and then tune the resonant frequency by shining thermal light (Thorlabs OSL2) onto the chip. The entangled probes are measured by two homodyne detectors. The photocurrents are filtered by high-pass filters (Thorlabs EF513), demodulated by an electrical mixer and amplified by a low-noise voltage preamplifier (Stanford Research Systems SR560). The data are acquired by an oscilloscope (LeCroy WavePro 604HD) at 1 MHz sampling rate for 20 s and post-processed to derive the individual and joint PSDs. The PSDs are obtained from fast Fourier transforms on the time-domain data averaged over 200 (400) oscilloscope traces, corresponding to an effective resolution bandwidth of 10 (20) Hz, as shown in Fig. 1 (Fig. 2). The measured PSDs at individual sensors are plotted in Supplementary Figs. 4 and 5.

Estimation of force resolution

The measured phase quadrature $Y_{\mathrm{out}}^{(i)}(t)$ at the two sensors is first converted into the equivalent sampled force $F^{(i)}(t)$ by the mechanical response functions. Then, individual sampled force $F^{(i)}$ is filtered by a band-pass filter within the 3 dB bandwidth $\mathcal{B}_{\mathrm{3dB}}$ during post-processing. The average joint force is given by $\bar{F}_{\mathrm{est}}(t)=(F^{(1)}(t)+F^{(2)}(t))/2$. The estimated force power at different times t_i is $E(t_i)=1/t_i\int_0^{t_i}\bar{F}_{\mathrm{est}}^2(t)\mathrm{d}t$. In the limit of weak signals $\delta^2\bar{F}_{\mathrm{sig}}\ll\delta^2\bar{F}_{\mathrm{N}}$, the statistical uncertainty of the estimator mainly arises from noise. Without the loss of generality, we only characterize the noise properties of our optomechanical sensors. To determine the accuracy of the power estimator, we recorded $J=20$ independent measurements of $\bar{F}_{\mathrm{N}}(t)$. Each measured trace gives an estimate of $E^{(j)}(t_i)$ with respect to acquisition time t_i up to 1 s. The root mean square error of the estimator is calculated by $\delta E(t_i)=\sqrt{\sum_{j=1}^{J}\left[E^{(j)}(t_i)\right]^2/J}$. The EFSR after t_i-second averaging, thus, reads

$$\delta F(t_i)=\sqrt{\delta E(t_i)}. \tag{4}$$

Two examples of the measured EFSR are presented in Fig. 5a,b.

Error analysis

We find that systematic errors dominate statistical fluctuations. Specifically, the systematic errors comprise the drifting in resonant frequency and optomechanical coupling rate. To derive systematic errors, we first fit the resonant frequencies $\Omega_{\{1,2\}}^{(k)}$ and optomechanical coupling rate $\beta_{\{1,2\}}^{(k)}$ of each sensor from K measurements to obtain the average resonant frequency $\bar{\Omega}_{\{1,2\}}=\sum_{k=1}^{K}\Omega_{\{1,2\}}^{(k)}/K$ and the average optomechanical coupling rate $\bar{\beta}_{\{1,2\}}=\sum_{k=1}^{K}\beta_{\{1,2\}}^{(k)}/K$, where $K=10$–15 depending on the specific experimental run. We then calculate the error of the measured bandwidth and minimum force noise with respect to the values calculated based on the average resonant frequency and optomechanical coupling rate as $\delta\mathcal{B}^{(k)}=|\mathcal{B}(\bar{\Omega}_{\{1,2\}},\bar{\beta}_{\{1,2\}})-\mathcal{B}(\Omega_{\{1,2\}}^{(k)},\beta_{\{1,2\}}^{(k)})|$ and $\delta S_{\bar{F}_{\mathrm{min}}\bar{F}_{\mathrm{min}}}^{(k)}=|S_{\bar{F}_{\mathrm{min}}\bar{F}_{\mathrm{min}}}(\bar{\Omega}_{\{1,2\}},\bar{\beta}_{\{1,2\}})-S_{\bar{F}_{\mathrm{min}}\bar{F}_{\mathrm{min}}}(\Omega_{\{1,2\}}^{(k)},\beta_{\{1,2\}}^{(k)})|$.

Data availability

The data that support the plots within this paper and other findings of this study are available from the corresponding authors upon reasonable request.

Code availability

The code used for modelling the data is available from Y.X. upon reasonable request.

Acknowledgements

Z.Z. acknowledges the Office of Naval Research (grant no. N00014-19-1-2190) for their support. Y.X., A.R.A., C.M.P., D.J.W., Q.Z. and Z.Z. acknowledge the National Science Foundation Convergence Accelerator award nos. 2040575 and 2134830. Y.X., A.J.B., Z.L., Q.Z. and Z.Z. acknowledge support from US Department of Energy, Office of Science, National Quantum Information Science Research Centers, Superconducting Quantum Materials and Systems Center (SQMS), under contract no. DE-AC02-07CH11359. Q.Z. acknowledges support from Defense Advanced Research Projects Agency (DARPA) under the Young Faculty Award (YFA) grant no. N660012014029 and NSF CAREER Award no. 2142882.

Author contributions

Y.X., D.J.W. and Z.Z. conceived and designed the experiments. Y.X. performed the experiments. Y.X., D.J.W. and Z.Z. analysed the data. A.R.A., C.M.P. and D.J.W. designed and fabricated the silicon nitride membrane devices. A.J.B., Z.L. and Q.Z. contributed to the analysis tools. Z.Z. supervised the project. All the authors contributed to the writing of the manuscript.

Competing interests

The authors declare no competing interests.

Additional information

Supplementary information The online version contains supplementary material available at https://doi.org/10.1038/s41566-023-01178-0.

Correspondence and requests for materials should be addressed to Yi Xia or Zheshen Zhang.

Peer review information *Nature Photonics* thanks the anonymous reviewers for their contribution to the peer review of this work.